Investigation of InAlN Layers Surface Reactivity after Thermal Annealings: A Complete XPS Study for HEMT

Y. Bourlier,[1,z] M. Bouttemy,[1] Olivier Patard,[2] Piero Gamarra,[2] S. Piotrowicz,[2] J. Vigneron,[1] R. Aubry,[3] S. Delage,[2] and A. Etcheberry[1]

[1]*Institut Lavoisier de Versailles, Université de Versailles Saint-Quentin en Yvelines, Université Paris-Saclay, 78035 Versailles Cedex, France*
[2]*Microelectronic GaN, III-V Lab, Campus Polytechnique, 91767 Palaiseau Cedex, France*
[3]*Thales Research & Technology, Campus Polytechnique, 91767 Palaiseau Cedex, France*

The surface chemistry of InAlN ultra-thin layers, having undergone an oxidation procedure usually running through the HEMT fabrication process (850°C, O_2 and O_2+Ar) is studied by XPS. The suitability of XPS analysis to operate as a retro-engineering tool for added value microelectronic devices fabrication is shown. A precise examination of the Al2p, In3d$_{5/2}$, N1s, and O1s peaks directly informs about spatial and atomic arrangement. The formation of a covering 3 nm surface oxide is evidenced after O_2 annealing. Once annealed, two specific additional N1s contributions are shown, at higher (404.0 eV) and lower binding energies (397.4 eV) compared to the InAlN matrix one (396.5 eV). To our knowledge, such fingerprint is rather unusual for ternary III-V materials. It reveals the formation of a nitrogen deficient interlayer, situated between the oxide overlayer and the undisturbed matrix, and the presence of interstitial N_2 molecules trapped at the interface. After Ar annealing, both oxide and interface layers are partially reorganized. InAlN reactivity toward higher annealing temperature (950°C) and its stability over time is finally discussed. N_2 molecules are unstable and progressively eliminated in time although nitrogen deficient interlayer still remains. Thermal treatments below 850°C are recommended to preserve the barrier chemical integrity.
© The Author(s) 2018. Published by ECS. This is an open access article distributed under the terms of the Creative Commons Attribution Non-Commercial No Derivatives 4.0 License (CC BY-NC-ND, http://creativecommons.org/licenses/by-nc-nd/4.0/), which permits non-commercial reuse, distribution, and reproduction in any medium, provided the original work is not changed in any way and is properly cited. For permission for commercial reuse, please email: oa@electrochem.org. [DOI: 10.1149/2.0181806jss]

Manuscript submitted April 19, 2018; revised manuscript received May 29, 2018. Published June 12, 2018. This was Paper 1412 presented at the Seattle, Washington Meeting of the Society, May 13–17, 2018.

III-V nitride materials combine unique properties such as a direct and tunable bandgap from N-IR (InN, 0.7 eV) to N-UV (AlN, 6.2 eV).[1] They are a matter of great interest for high performance in electronic and optoelectronic devices such as light emitting diodes,[2,3] Bragg reflectors,[4,5] cladding layer in lasers,[6] high efficiency solar cells[7] and also HEMT (High Electron Mobility Transistors) for power electronics and RF amplifiers from S-Band up to sub-millimeters wave applications.[8,9] Among the electronic devices, the GaN based technology is very suitable for high frequency operations such as satellite communications. AlGaN/GaN device structures are commonly developed for HEMTs devices,[10] offering high performances. The main drawback of this technology is the lattice mismatch between the AlGaN and the GaN, leading to a significant stress in the barrier layer.[11] Moreover, during device operation, an additional stress due to inverse piezoelectric effect is locally induced by the high electric field.[12]

More recently, InAlN/GaN structures are a matter of great interest.[13] The strong advantage of $In_xAl_{1-x}N$ is a spontaneous high charges polarization leading to an extremely high carrier density in the two-dimension electron gas (2DEG), up to 3.5×10^{13} cm^{-2}, which cannot be achieved with traditional AlGaN/GaN structures.[14–17] Besides, the near lattice matched composition with GaN is achieved for x = 0.17–0.20, leading to a strain-free heterojunction which drastically reduces the structural defects.[8,18,19] The main difficulty resides in making a high crystalline quality and a good homogeneity of InAlN layers,[20,21] InN and AlN suffering from a large difference of covalent bond, resulting from phase separation and strong spinodal decomposition.[22,23] Nevertheless, MBE[24–26] and also MOVPE[27,28] are both leading to excellent composition uniformity and good device performances with thin-layer engineering around 7 nm of thickness.[8,29]

During the fabrication process of the HEMT, the InAlN/GaN layers have to go through different steps: (1) chemical treatments to prepare the surface, (2) voluntary oxidation at high temperature under O_2 oxygen and Ar, (3) Ti/Al/Ni/Au/Ti/Pt ohmic contacts stack deposition (e-gun evaporation) followed by a thermal annealing (> 800°C) under N_2 atmosphere, (4) oxide layer openings and Ar+ implantation for device electrical isolation before E-beam lithographed T-gates contact (Ni/Pt/Au metal stack) deposition (e-gun evaporation), and (5) passivation of the device with a 150-nm thick Si_3N_4 film deposited by plasma enhanced chemical vapor deposition (PECVD). Additional metallization steps are also realized to complete the devices.

As all nitride materials provide an efficient diffusion barrier against oxygen, III-V nitride materials are known to be highly chemically stable at working temperature and poorly reactive to air exposure. InAlN/GaN HEMT structure has been shown to be stable and operate with success at high temperature until 1000°C at the lattice match composition with the use of suitable passivation layers.[30–32] Nevertheless, InAlN surface modification can be observed during the thermal annealing performed to bring a good ohmic contact.[33] Such superficial chemical variations can harm the quality of 2DEG density, decreasing also the electron mobility and the sheet carrier density when temperatures above 800°C are employed.[34–36] On the basis of previous considerations, if we consider binary compounds separately, AlN is known to be stable up to 1250°C,[37] whereas InN is known to be stable up to 550°C[38–40] and decomposes above this temperature into N_2 and liquid In. Only few studies concern the chemical stability of InAlN layers through annealing temperatures. J. Palisaitis et al. have done deep investigations by STEM (Scanning Transmission Electron Microscopy) characterization on InAlN thin layers during in situ thermal annealing.[41,42] Their work points out the fact that In-rich layers decompose at 750°C, starting from the formation of metallic In clusters at grain boundaries, whereas Al-rich layers show few signs of decomposition and remain chemically stable even at 950°C. Consequently, different approaches are considered by the community, such as operating at slower growth rate in MOVPE to increase thermal stability,[43] or processing ohmic contact at a lower annealing temperature around 600°C.[44–46] Actually, the growth of a thermal oxide layer on III-V nitrides like InAlN is still hard to control and not fully understood.

Another way to protect InAlN barrier surface from degradation is to intentionally oxidize the surface by performing a thermal annealing of more than 800°C under O_2 before making the ohmic contacts. In fact, different studies show that the thermal oxidation can be employed as a useful tool generating a nearly beneficial native Al_2O_3 oxide layer serving as an insulating layer, reducing the gate leakage current and

[z]E-mail: yoan.bourlier@uvsq.fr

Downloaded on 2018-09-14 to IP 193.51.24.15 address. Redistribution subject to ECS terms of use (see ecsdl.org/site/terms_use) unless CC License in place (see abstract).

improving performances.[47–50] Though, there is still a strong need to deeply investigate the influence of the thermal budget in order to orient and control the fabrication process. Indeed, a precise knowledge of the InAlN layer surface chemistry under this process of oxidation is required to ensure the final quality and high performances of the HEMT device. By its general escape depth of 10 nm, X-ray Photoelectron Spectroscopy (XPS) an extremely well-suited analysis method to investigate the surface and interface chemistry evolution of ultra-thin InAlN layers.

In the present paper, the surface analysis of Al-rich and lattice match layers of $In_{0.2}Al_{0.8}N$, grown by MOVPE and presenting a thickness of 7–8 nm is implemented by XPS. Thus, an XPS monitoring of the surface chemistry will be performed starting from the initial ammonia treatment, employed as a preliminary deoxidation treatment to prepare the InAlN surface, then after a following thermal treatment under O_2-rich atmosphere at 850°C, known as an oxidation step and performed during the process in order to limit the leakage current, and finally after an additional Ar atmosphere annealing at 850°C, acting as a stabilization step before cooling.

A detailed examination of, first, the overall XPS survey spectra, and second, the high energy resolution XPS spectral regions with complete peak fitting of N1s, Al2p, $In3d_{5/2}$, and O1s core-levels, will be presented. Evolution of atomic concentrations and chemical environment differentiations between the covering oxide layer and the matrix below will be discussed for each process step. An oxide film growth mechanism will be proposed with respect to the specific composition of the oxide layer. Indeed, not only N1s contribution of the InAlN matrix (397.4 eV) will be identified but also two uncommon additional contributions at lower (396.5 eV) and more surprisingly at higher (404.0 eV) binding energy. The two last contributions, referred as secondary phases, will be precisely identified. Their proportion evolutions will be also discussed through a higher O_2 thermal annealing at 950°C, and through ageing time (of two months and then of one year).

We believe that a key point for high performances HEMT is to achieve the understanding of how InAlN surface layers can react through the oxidation procedure and how its surface chemistry evolution can be stable. The present publication, thanks to XPS expertise, especially brings new insights on InAlN/GaN based structure chemical modifications amplified during temperature O_2 and Ar annealing (850–950°C, step (2)).

Experimental

The samples were prepared at III-V Lab using an Aixtron AIX200RF horizontal MOVPE reactor. The heterostructures, grown on semi-insulating 4H-SiC substrates consist of a 1.8-µm thick insulating GaN buffer layer followed by a 1.5-nm thick AlN interlayer and an InAlN barrier with an In content of 20 %, as measured by X-Ray diffraction analyses, and a thickness of 7 nm, as measured by X-Ray reflectivity. Prior to the thermal oxidation step, the native ultra-thin oxide film present at the surface of the samples were removed using an ammonia based wet etching (NH_4OH) as referred in other works on AlGaN[51] or InAlN[52,53] materials. This step will be considered as bringing the InAlN surface reference for XPS and corresponds subsequently to Sample 1 notation. Sample 2 has been cleaned in the same way than Sample 1 and was then annealed under dioxygen (O_2) flux at 850°C for 1 min with a controlled pressure of 5.0 10^{-1} Pa. This step with an exceeding temperature, intend to increase the thickness of the oxide at the InAlN surface. Sample 3 was annealed in the same way than Sample 2 and has been additionally submitted to a thermal annealing under Argon (Ar) flux at 850°C for 1 min with a controlled pressure of 2.3 10^{-1} Pa. These thermal treatments are implemented to reach high performances and becoming an essential part of the HEMT fabrication process. The three samples have been then transferred immediately and at the same time into the XPS spectrometer without specific care to air contamination.

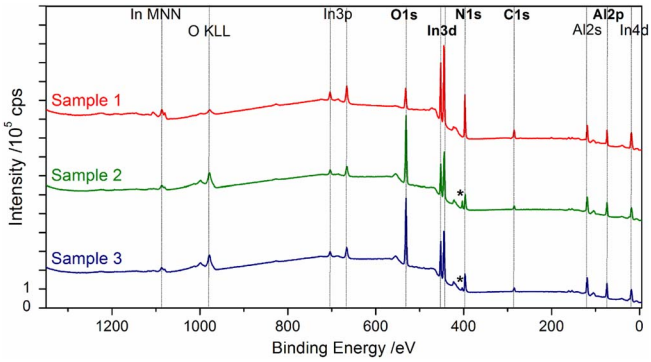

Figure 1. XPS survey spectra representative of as-grown InAlN after NH_4OH cleaning (Sample 1), further O_2 thermal annealing at 850°C (Sample 2), and additional Ar thermal annealing at 850°C (Sample 3). The spectral windows of O1s, In3d, N1s, C1s, and Al2p, are the ones considered for the quantification and the fitting procedure presented in the next part. The "*" typing corresponds to a specific additional N1s feature.

The thickness of the surface oxide was measured by TEM (Transmission Electron Microscope) on Sample 2 (annealed under O_2 flux at 850°C) formerly prepared by FIB (Focus Ion Beam).

To enhance the surface modification of InAlN layers, presenting high stability and low reactivity,[16,30,32] another sample having undergone a higher thermal budget was prepared. This sample was cleaned under the same procedure and annealed at 950°C for 1 min under the same O_2 flux, noted Sample 2bis, and also additionally annealed at 950°C for 1 min under the same Ar atmosphere, noted Sample 3bis. Finally, to address the question of the InAlN barrier stability after annealing step, the annealed samples were analyzed, after two months air ageing at room temperature (thereby Sample 2 and Sample 3) and one year (Sample 3bis).

The surface chemical composition and chemical environments evolutions were accurately characterized by XPS (X-ray Photoelectron Spectroscopy). XPS experiments were carried out with a Thermo Electron K-Alpha spectrometer equipped with a monochromated Aluminium (Al) Kα X-ray source (1486.6 eV) and a hemispherical analyzer operating at normal acceptance in the Constant Analyze Energy mode (survey: 200 eV and high energy resolution spectral windows: 50 eV). Spot sizes are typically 400µm. XPS mapping were performed using multi-point detection mode. Surface charging effect was compensated by using an Ar^+ flood gun and the energy scale was calibrated with reference to the C1s peak position at 284.8 eV, characteristic of C-C bonds present in adventitious carbon. The Thermo Electron K-Alpha spectrometer procedure was used to calibrate the spectrometer and verified using copper (Cu) and gold (Au) samples following the ASTM-E-902-94 standard procedure.

The Thermo Avantage software was used for quantification and N1s, Al2p, In3d5/2, and O1s photopeaks reconstruction procedure using a Shirley background subtraction and a convolution of Gaussian-Lorentzian mix product function with L/G = 30%. The corresponding atomic concentrations were calculated from corrected peak areas using relative sensitivity factors (RSF) and transmission function of the spectrometer provided in the Thermo Avantage software. The fitting procedure developed on standard fully deoxidized InP and AlGaAs reference spectra, acquired in the same experimental conditions, was implemented on present InAlN spectra to ensure an accurate differentiation between oxide phases and the InAlN matrix.

Results and Discussion

Observation of the overall chemical compositions using the XPS survey spectra.—The high homogeneity of the InAlN layers chemical surface composition is assessed by the good correlation of the different XPS results. Indeed, a statistical study was done with distinct analysis points randomly scattered on the surface of each samples

Downloaded on 2018-09-14 to IP 193.51.24.15 address. Redistribution subject to ECS terms of use (see ecsdl.org/site/terms_use) unless CC License in place (see abstract).

Table I. Atomic concentrations of Al, In, N, O and C, obtained from the XPS survey spectra of the Samples 1 to 3. The standard deviation is inferior to 0.2 at.%. (*) See explanation in caption Figure 1.

		Al2p	In3d$_{5/2}$	N1s / N1s(*)	O1s	C1s
Sample 1	InAlN as-grown + NH_4OH cleaning	25.9%	5.9%	33.1%/0.0%	19.4%	15.7%
Sample 2	O_2 annealing (850°C)	29.9%	3.6%	10.8%/5.4%	44.4%	6.0%
Sample 3	Additional Ar annealing (850°C)	30.3%	3.9%	14.3%/2.1%	43.9%	5.5%

which demonstrates, as expected, the reproducibility of XPS spectra, and so, the uniformity of the InAlN surfaces (not presented here). The elementary composition determined over the different areas remains constant. Representative survey spectra of Samples 1, 2, and 3, are presented in Figure 1 and the extracted overall XPS atomic concentrations of the main elements are given in Table I with a standard deviation of less than 0.2 at.% for all data.

Regarding from these spectra, Silicon (Si) signals are also found on the samples with a maximum total amount around 4 at.%. Such Si residual content corresponds to a cleavage artefact, the samples being cut from the same wafer onto approximatively 1 × 1 cm^2 pieces for XPS analysis convenience and some SiC back-side residues being redeposited on the front surface. We choose, to be conform to the original fabrication process and to preserve the InAlN as-grown surface composition, to directly immerse the samples in NH_4OH after cutting, without mechano-chemical cleaning which would have eliminated the Si residues.

The comparison of the XPS surface composition of Samples 1, 2 and 3 (Table I) evidences a modification after the annealing steps of InAlN. The carbon contamination is drastically decreased from 15.7 at.% on the as-grown (Sample 1) to unconventional low carbon content for samples transferred without special care to atmosphere exposure, around 6.0 at.% (Sample 2) and even less (Sample 3). These very weak values are consistent with the results of King et al.[54] concerning the thermal oxidation of similar III-V nitride surfaces (AlN and GaN). It reveals very specific surface properties concerning its poor adventitious carbon sticking, and leading to a high surface stability with regard to air atmosphere contact and associated contamination.

For the main chemical elements Aluminium (Al), Indium (In), Nitrogen (N) and Oxygen (O), a clear modification of the atomic balances is also observed before and after the oxidation process. Comparing Sample 2 to Sample 1, a strong increase in O content, from 19.4% up to 44.4%, is measured and evidences the growth of an oxide film at the InAlN surface. This O enrichment is well visible on the survey spectra (Figure 1) when comparing the evolution of the O1s peak and the Auger O-KLL bands. This increase of O content is also correlated to a decrease in the N one, from 33.1% down to 10.8%, this element being not involved in the oxide film network, and also in In whose content varies from 5.9 % down to 3.6%. Moreover, the Al content increases, from 25.9% up to 29.9%. This indicates that the oxide film is Al-rich, what is consistent with the high oxygen affinity of this element. Minor composition changes are observed after Ar annealing (Sample 3), the final thermal treatment having practically no effect on the chemical composition of the oxide layer grown in the previous step.

To get more precise insight on the surface composition modifications, characteristic ratios are presented in Table II. It reveals a high increase of the III/V element balance: "(Al+In)/N" after annealing (Sample 2 and 3), reaching 3.1 on Sample 2, compared to the one measured on the reference metal-nitride matrix (Sample 1),

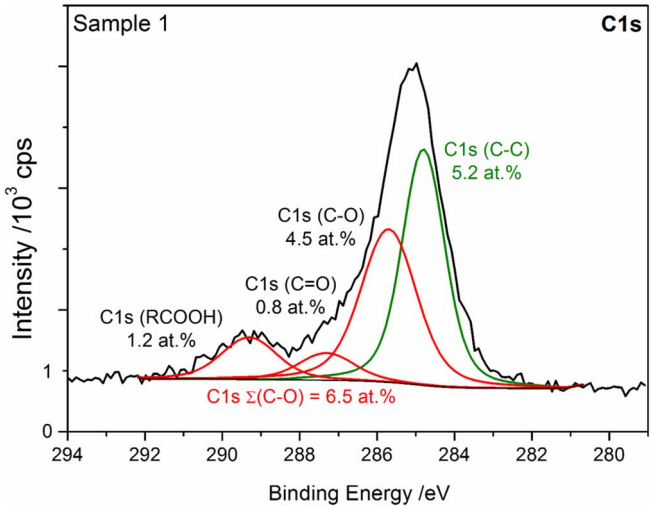

Figure 2. High energy resolution XPS spectrum of C1s region on Sample 1: (C-C), (C-O), (C=O) and (RCOOH) bonds are well-distinct inside the adventitious carbon content. Σ(C-O) is related to the addition of all carbon attributions associated to at least one oxygen atom (see Tables III and IV).

as expected close to 1. This increase of the III/V balance indicates a consequent change at the surface of the InAlN layer. Moreover, an additional feature, pointed "*" in Figure 1, appears in the N1s region of the two samples annealed at higher binding energy than usual N1s photopeak position for nitride compounds (at 397.4 eV). This peak observed at 404.0 eV is not taken into account in all the characteristic ratio determination, as it cannot be attributed to N in the InAlN matrix network (Table II). One should note that its content is reduced after the Ar annealing (Table I). This specific XPS signature of the N1s photopeak will be investigated in more details below.

The O involved in the oxide film network, noted "Oox", can be estimated after deduction of O linked to the carbon contamination from the total O content. The fit of the C1s spectrum (Figure 2) enables to determine this corrective value, and leads to an equivalent proportion between the "C-C" and "C-O" environments, so the estimation can be provided using "[Oox] = [O]-[C]/2". Considering the very low carbon content in the present case, especially for Sample 2 and Sample 3, this approximation only has a low effect on O value.

The ratio between the overall III-elements content and "Oox", "(Al+In)/Oox", is drastically decreased from 2.05 (Sample 1) to 0.81 (Sample 2), in accordance with the increase of O content and then remains stable at 0.83 (Sample 3) after Ar annealing. The matrix is still visible (N presence) and this ratio also takes into account the Al and In proportion associated to the matrix below. The oxide

Table II. Characteristic ratios evolution obtained from the XPS survey spectra of the Samples 1 to 3. The standard deviation is assumed at ± 0.02. "Oox" is the oxygen content corrected from associated carbon contamination.

		(Al+In)/N	(Al+In)/Oox	In/(Al+In)	(Al+In)/(N+Oox)
Sample 1	InAlN as-grown + NH_4OH cleaning	0.96	2.75	0.19	0.71
Sample 2	O_2 annealing (850°C)	3.10	0.81	0.11	0.64
Sample 3	Additional Ar annealing (850°C)	2.39	0.83	0.11	0.62

Downloaded on 2018-09-14 to IP 193.51.24.15 address. Redistribution subject to ECS terms of use (see ecsdl.org/site/terms_use) unless CC License in place (see abstract).

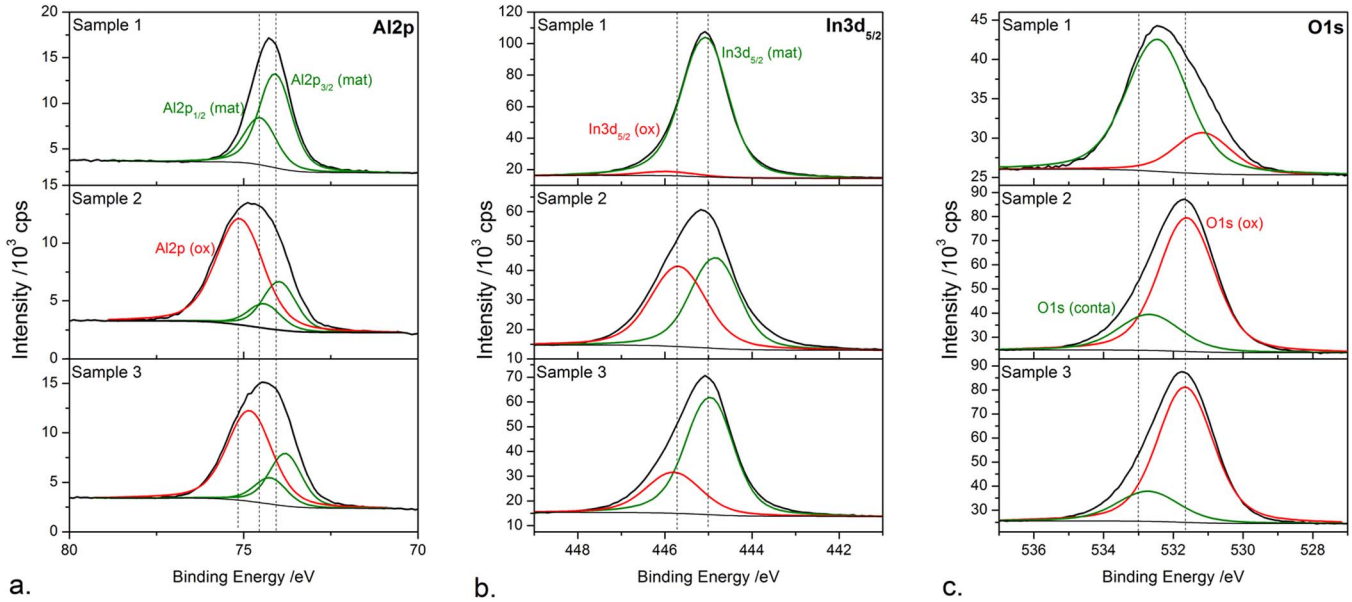

Figure 3. Reconstruction of the high energy resolution XPS spectra of a. Al2p, b. In3d$_{5/2}$, and c. O1s regions for as-grown InAlN after NH_4OH cleaning (Sample 1), further O_2 thermal annealing at 850°C (Sample 2), and additional Ar thermal annealing at 850°C (Sample 3). InAlN matrix contribution named "(mat)", oxide top layer contribution named "(ox)", and superficial contamination named "(conta)" for oxygen content assigned to carbon contamination.

composition will be refined after proceeding to the reconstruction of the high energy resolution spectra, enabling to separate oxide and matrix contributions, detailed in the next paragraph.

Furthermore, the substitution rate of In, "x = In/(Al+In)", obtained by XPS is 19% and is in good accordance with the XRR value of 20% measured on the InAlN as-grown film (Sample 1), attesting of the good lattice match with GaN.[8] This ratio then declines to 11% after thermal annealing (Sample 2 and Sample 3) revealing an In depletion within the depth probed by XPS. Finally, the overall ratio, "(Al+In)/(N+Oox)" shows practically no evolution and remains relatively constant between 0.6 to 0.7, showing that the overall content of elements is conserved. The study of high energy resolution spectra will emphasize these preliminary results.

XPS peak fitting of high energy resolution spectra and interpretation of InAlN thin film oxidation after O_2 thermal annealing and additional ar thermal annealing.—The spectral regions of interest: Al2p, In3d$_{5/2}$, and O1s are presented in Figure 3. Evolutions of the high energy resolution XPS spectra shapes are correlated to strong modifications previously suggested from survey examination. Firstly, it can be settled that binding energy (BE) of the overall envelopes of Al2p and In3d$_{5/2}$ (observed at Figures 3a and 3b.) are modified after O_2 annealing (Sample 2) showing an increase of the full width at half maximum (FWHM) of the peaks. This is due to the rise of another contributions at higher energy (named "(mat)") compared to the matrix ones (named "(mat)"), and consistent with the surface oxidation previously presented with the corresponding survey spectra analysis. At the same time, the shoulder of the O1s photopeak observed on the reference (Sample 1) changes after O_2 annealing by shifting the global position to lower energies (Sample 2) indicating a reversal between the contamination (named "(conta)") and oxide (named "(ox)") contributions preponderance (Figure 3c).

The N1s spectra windows of the three samples are gathered in Figure 4. A very specific XPS response is shown after the annealing steps (on Samples 2 and 3), with the appearance of a new and unusual contribution at 404.0 eV, thereafter named "(inter)", in addition to the expected "(mat)" one around 397.3 eV, representative of the matrix.

The spectroscopic parameters, calibrated binding energy (BE) and peak's width (FWHM), employed for the reconstruction procedure of the different spectral windows are gathered in Tables IIIa. and IIIb. respectively. Corresponding atomic concentrations for the differentiated components are gathered in Table IV.

First of all, the fitting procedure of Sample 1 is detailed as it will be representative of the initial reference configuration. As obtained with the reference standard AlGaAs for Al2p (previously introduced in the experimental part), a slight asymmetry of the peak envelope is considered to take into account the Al2p spin orbit coupling of 0.44 ± 0.01 eV. Indeed, Al2p$_{3/2}$ and Al2p$_{1/2}$ peaks are fitted with the same line shapes, the same FWHMs (assumed at 1.10 ± 0.02 eV), and with a 2:1 area ratio, as constraints. The optimized value of the spin orbit splitting is also in perfect agreement with other works related to AlN.[55,56] The main "Al2p$_{3/2}$ (mat)" contribution is positioned at 74.0 ± 0.2 eV. A similar value was previously reported for AlN[57,58] environment and attributed to Al atoms in InAlN bulk material. The

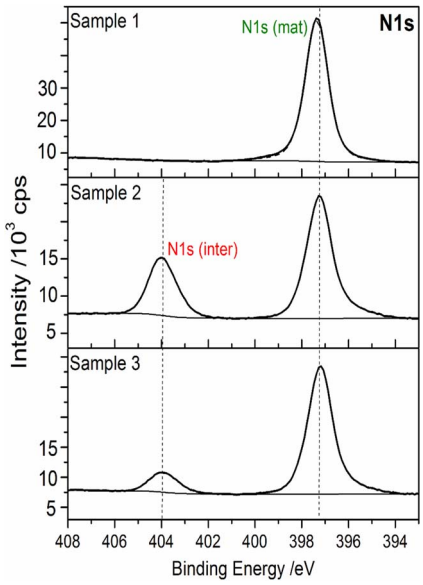

Figure 4. High energy resolution XPS spectra for N1s region of Sample 1, 2, and 3: "(mat)" peak is associated to the InAlN matrix and "(inter)" to the additional peak monitored for Sample 2 and 3.

Downloaded on 2018-09-14 to IP 193.51.24.15 address. Redistribution subject to ECS terms of use (see ecsdl.org/site/terms_use) unless CC License in place (see abstract).

Table III. a. Calibrated values of Binding Energy (BE) and b. Simulated values of Full Width at Half Maximum (FWHM) during the fitting procedure of Al2p, In3d$_{5/2}$, N1s, O1s, and C1s spectral windows, for Samples 1, 2 and 3, associated to Figures 2, 3, and 4. The standard deviation is assumed at ± 0.2 eV for the BE, and at ± 0.05 eV for the FWHM.

	BE /eV				FWHM /eV		
a.	Sample 1	Sample 2	Sample 3	b.	Sample 1	Sample 2	Sample 3
Al2p$_{1/2}$ (mat)	74.5	74.4	74.2	Al2p$_{1/2}$ (mat)	1.10	1.12	1.11
Al2p$_{3/2}$ (mat)	74.1	74.0	73.8	Al2p$_{3/2}$ (mat)	1.10	1.12	1.11
Al2p (ox)	/	75.1	74.8	Al2p (ox)	/	1.60	1.51
In3d$_{5/2}$ (mat)	445.1	444.8	445.0	In3d$_{5/2}$ (mat)	1.20	1.25	1.23
In3d$_{5/2}$ (ox)	446.0	445.7	445.8	In3d$_{5/2}$ (ox)	1.46	1.50	1.49
N1s (mat)	397.4	397.3	397.2	N1s (mat)	1.20	1.20	1.20
N1s (inter)	/	404.0	403.9	N1s (inter)	/	1.40	1.44
O1s (ox)	531.2	531.6	531.7	O1s (ox)	1.90	1.90	1.90
O1s (conta)	532.5	532.7	532.7	O1s (conta)	2.10	2.10	2.10
C1s (C-C)	284.8	284.8	284.9	C1s (C-C)	1.30	1.30	1.30
C1s Σ(C-O)	285.7-289.3	285.7-289.3	285.7-289.3	C1s Σ(C-O)	1.70	1.70	1.70

peak reconstruction procedure of Al2p, well satisfactorily fit the experimental envelope. It suggests that the residual oxide remaining on surface is principally or only constituted of In oxide, although the possibility of a minor "Al2p (ox)" contribution can be comprised within the error bar of the fit. The "In3d$_{5/2}$ (mat)" contribution is positioned at 445.0 ± 0.2 eV. This chemical shift is close to the one observed on InN.[59-61] A "In3d$_{5/2}$ (ox)" contribution, settled with a positive shift of 0.9 ± 0.1 eV from the "In3d$_{5/2}$ (mat)" energy position, is found in a very low proportion on Sample 1 (only 0.2 at.% of In).

Indeed, owing to its low O content, Sample 1 appears as an almost fully deoxidized layer. The most part of the O1s signal, positioned at 532.5 ± 0.2 eV, is assigned to superficial carbon contamination "O1s (conta)",[62] and clearly shows that the residual oxide cannot be totally covering. By the way, the O content related to the oxide, "O1s (ox)" appears clearly overestimated for the Sample 1 (at 4.2 at.% in Table IV). Regarding from the low atomic content of In and Al oxide, we assume that this discordance is due to side silicon oxide present at the surface as already explained in the previous part.

The N1s region of Sample 1 presents only one component, "N1s (mat)" (Figure 4), positioned at 397.4 ± 0.2 eV. This value is in good agreement with tabulated ones for InAlN[63] and AlN[57,58] nitrides, enabling us to attribute this contribution to N atoms implied in the InAlN matrix. Finally, "Al2p$_{3/2}$ (mat)", "In3d$_{5/2}$ (mat)", and "N1s (mat)" can be clearly assigned to Al, In, and N atoms inside the InAlN matrix. Moreover, their respective FWHMs, 1.10 eV, 1.20 eV, and 1.20 eV (Table IIIb.) are consistent, suggesting a unique and stable InAlN network for the Sample 1. Furthermore, the interband energy differences of the matrix contributions presented as follow: "ΔBE (N1s/Al2p$_{3/2}$) = 323.3 eV", "ΔBE (In3d$_{5/2}$/N1s) = 47.7 eV", and "ΔBE (In3d$_{5/2}$/Al2p$_{3/2}$) = 371.0 eV", are in good agreement with values published in previous works on InAlN as-grown layer.[63]

After annealing (Sample 2 and 3), an increase of the O1s contribution, situated in an energy range characteristic of O present in oxide compounds[56] ("O1s (ox)"), is shown and positioned using a positive shift of 1.2 ± 0.2 eV with a FWHM of 1.9 ± 0.02 eV. The "O1s (ox)" contribution rises from 4.2 at.% in Sample 1 to about 37.0 at.% in Sample 2 and 3. Precisely, we assume that these values are overestimated of about 4 at.% with respect to the fraction of silicon oxide revealed by the survey spectra. Additionally, a concomitant contribution at higher binding energy is required to reconstruct the envelopes of Al2p and In3d$_{5/2}$ photopeaks and corresponds to the formation of a covering oxide top layer (Figure 3). A unique component "Al2p (ox)" is added to the fit, and positioned using the same positive shift of 1.1 ± 0.1 eV (from the "Al2p$_{3/2}$ (mat)" energy position) and with a FWHM of 1.60 eV (Sample 2) and 1.50 eV (Sample 3). "Al2p (ox)" proportion rises from almost 0.0 at.% (Sample 1), to 19.4 at.% (Sample 2), and to 18.4 at.% (Sample 3). Concerning the oxide contribution in the In3d$_{5/2}$ region, the "In3d$_{5/2}$ (ox)" peak is positioned using similar condition than Sample 1 using a positive shift of 0.9 ± 0.1 eV and with a FWHM of 1.50 ± 0.02 eV. "In3d$_{5/2}$ (ox)" proportion also rises from 0.2 at.% (Sample 1), to 2.0 at.% (Sample 2), and to 1.2 at.% (Sample 3). Any details about the precise attributions of the chemical bonds Al-O and In-O (hydroxides and suboxides for instance) would be rather difficult and will not be discussed in this study. Nevertheless, the energy positions of "Al2p (ox)" and "In3d$_{5/2}$ (ox)" are consistent with the one measured for Al_2O_3[56,58] and for In_2O_3-like oxide[60,61] respectively.

In the N1s region, a main prominent "N1s (mat)" peak (Figure 4) is still visible but an additional structure at 404.0 ± 0.2 eV emerges. According to the literature, this additional peak can be assigned at first sight to interstitial N containing molecules (N_2 or NO_x),[64] probably trapped inside the structure, and thereafter named "N1s (inter)". The atomic concentrations of the "N1s (inter)" for Sample 2 and 3 are

Table IV. Differentiated XPS atomic concentrations obtained after reconstruction of Al2p, In3d$_{5/2}$, N1s, O1s, and C1s, photopeaks for the three samples (cf Figures 2, 3, and 4). The standard deviation is assumed at ± 0.1 at.%.

	Atomic concentrations/at.%		
	Sample 1	Sample 2	Sample 3
Al2p (mat)	27.7	9.3	11.6
Al2p (ox)	0.0	19.4	18.4
In3d$_{5/2}$ (mat)	6.8	2.0	3.0
In3d$_{5/2}$ (ox)	0.2	2.0	1.2
N1s (mat)	34.5	11.8	14.9
N1s (inter)	0.0	5.5	2.3
O1s (ox)	4.2	36.6	37.1
O1s (conta)	15.1	11.0	9.2
C1s (C-C)	5.2	1.0	1.0
C1s Σ(C-O)	6.4	1.5	1.5

Table V. Characteristic ratios of the three samples, describing the InAlN matrix and the oxide layer composition after the thermal annealings. The standard deviation is assumed at ± 0.01.

	Characteristic ratios		
	Sample 1	Sample 2	Sample 3
[In (mat)+Al (mat)]/N (mat)	1.00	0.96	0.98
In (mat)/[Al (mat)+In (mat)]	0.20	0.18	0.21
[Al (ox)+In (ox)]/O (ox)	0.06	0.59	0.53
In (ox)/[Al (ox)+In (ox)]	/	0.09	0.06
Al (ox)/Al (mat)	0.00	2.08	1.58
In (ox)/In (mat)	0.04	1.01	0.40
C-C/Σ(C-O)	0.81	0.65	0.65

Downloaded on 2018-09-14 to IP 193.51.24.15 address. Redistribution subject to ECS terms of use (see ecsdl.org/site/terms_use) unless CC License in place (see abstract).

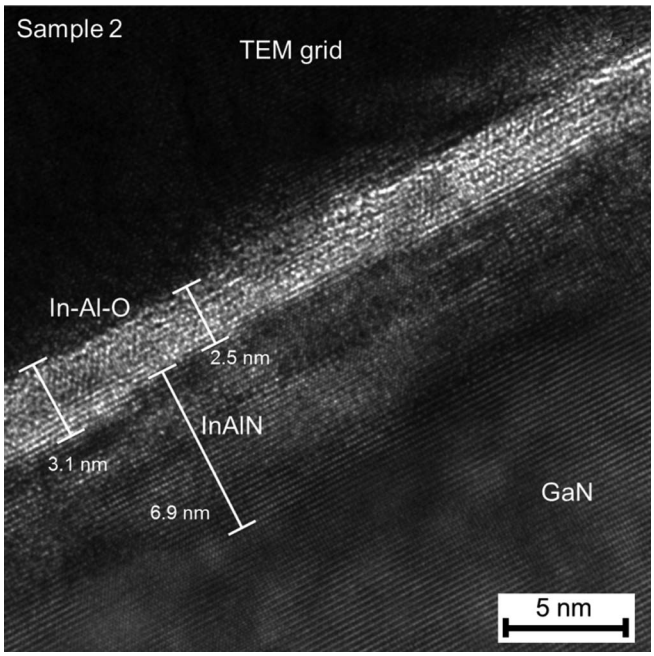

Figure 5. TEM cross section of InAlN layer annealed under O_2 at 850°C (Sample 2). Thickness measurement of the surfacing oxide layer (In-Al-O) is shown and ranged between 2.5 and 3.1 nm.

found to be 5.5 at.% and 2.3 at.% respectively (Table IV). Besides, another contribution at lower energy and named "N1s (N<1)", included inside the "N1s (mat)" contribution, is evidenced in the annealed samples. Its evolution will be detailed in the next part.

The characteristic ratios of the InAlN matrix and the Indium-Aluminium oxide layer, "In-Al-O", are presented in Table V. The InAlN atomic ratio on the reference sample (Sample 1) after peak reconstruction, "[In (mat)+Al (mat)]/N (mat) = 1.00", is in total agreement with the value calculated with overall contents coming from the survey spectra: "(Al+In)/N = 0.96" (Table II), validating the fitting procedure. In addition, the oxide content for Sample 1 is extremely low, only 0.2 at.% of In, and confirms that almost all the XPS signal collected is coming from the InAlN matrix. It also attests the presence of a non-covering and ultra-thin oxide coming from a very small remaining fraction of the native In oxide.

After annealing steps, oxidation has been clearly evidenced. Consequently, the oxide ratio, "[Al (ox)+In (ox)]/O (ox)" at Table V, increases substantially by a factor of 10, rising from 0.06 before annealing, to 0.59 after O_2 annealing, and to 0.53 after the subsequent Ar annealing. This characteristic ratio of the oxide over layer is lower than the 0.67 one expected for a mixed oxide of Al_2O_3 and In_2O_3. Despite the slightly overestimated "Oox" contribution (as previously explained), we can also assume the existence of a proper and covering mixed "In-Al-O" oxide structure, particularly Al rich.

The thickness of the oxide overlayer is evaluated on a TEM (Transmission Electron Microscopy) cross section image. A conformal oxide layer presenting a thickness comprised between 2.5 and 3.1 nm is measured for oxidized samples (Figure 5).

This thickness can also be estimated from XPS data. As the oxide layer is composed of more than 90 % of Al oxide, the thickness calculation is done by simplifying the model considering only an Al_2O_3 superficial layer covering the barrier layer. A rigorous approach would also consider the attenuation of Al2p signals by superficial adventitious carbon contamination, considered equivalent for all the samples here (low C contents) and then neglected in the present calculation. First, the TPP-2 M equation[65,66] is used to calculate the theoretical IMFP (Inelastic Mean Free Paths of photoelectrons) parameter "λ_{ox}" and is found around 3.0 ± 0.1 nm. Then, the oxide layer thickness "d_{ox}" is determined using the following relation based on XPS signal attenuation: "$d_{ox} = \lambda_{ox}.\ln(I_0/I)$", with "$I_0$" the relative intensity of "Al2p (mat)" measured on the reference (Sample 1) and "I" the relative intensity of "Al2p (ox)" measured on oxidized samples (Sample 2 and 3). Finally, the estimated thicknesses are found between 2.6 and 2.8 nm for Sample 2, and between 1.9 and 2.0 nm for Sample 3. These values are in good agreement with the TEM measurement. It can also confirm that the oxide layer is thinner after the Ar thermal treatment leading to a possible re-arrangement inside the oxide layer and the interface.

To get into more details about the oxidation mechanism, we can first observe that the overall In content decreases (Tables II and IV) by almost a factor of 2 from Sample 1 to Sample 2. Indeed, pure InN can start to decompose above 600°C[39,67] and the present thermal budget is sufficient to cause In loss inside the ternary alloy. Additionally, both "In$3d_{5/2}$ (ox)" and "In$3d_{5/2}$ (mat)" contributions are impacted. Both oxide formation and In loss are observed during the thermal annealing, and N is not involved in the oxide network, so, an associated N loss is observed as well as a modification of its distribution in depth. Indeed, the overall N content "N1s (mat)+N1s (inter)" decreases from 34.5 ± 0.1 at.% (Sample 1) to about 17.2 ± 0.1 at.% (Sample 2 and 3). Nevertheless, the atomic balance in the matrix beyond the oxidation film is not significantly modified. The global ratio "[In (mat)+Al (mat)]/N (mat)" only slightly decreases from 1.00 on the reference surface practically oxide free (Sample 1) to 0.96 (Sample 2) and 0.98 (Sample 3) after their respective annealings. These results point out the existence of an ultra-thin perturbed layer on top of the InAlN matrix, just beyond the oxide top layer, noted "$In_yAl_{1-y}N_{(<1)}$", caused by the thermal oxidation treatment. This interlayer is assumed to be deficient in In and N.

As for In and Al, the total N quantity remains practically unchanged after Ar annealing. For Al, the "Al (ox)/Al (mat)" ratio slightly declines from 2.08 (Sample 2) to 1.58 (Sample 3), with the Al oxide contribution remaining clearly predominant (Table V). Concerning In, a more notable decrease of the "In (ox)/In (mat)" ratio is observed, varying from 1.01 (Sample 2) to 0.40 (Sample 3), and showing an inversion of predominance of the contributions after Ar annealing. Thus, a slight decrease of the In content in the oxide, going from 9% to 6% for the "In (ox)/[Al (ox) + In (ox)]" ratio, is associated to an increase of the In content inside the matrix, from 18% to 21% for the "In (mat)/[Al (mat) + In (mat)]" ratio, recovering the initial In content (Sample 1). As the In contents remain roughly constant for Sample 2 and 3, the Ar annealing seems to act as a reducing agent for In oxide, probably causing a structure rearrangement at the interface between the oxide and the matrix. Finally, the N associated to the InAlN matrix, "N1s (mat)", is found to increase from 11.8 at.% to 14.9 at.% after the Ar annealing (Table V); and conversely, the N1s proportion related to the interstitial N content, "N1s (inter)", decreases from 5.5 at.% to 2.3 at.%. We can also assume that Ar thermal treatment not only reduces the oxide layer thickness, but also leads to a restructuration of the interlayer inside the InAlN matrix.

To summarize, a simple and direct oxidation mechanism of InAlN surface is excluded for which the initial metallic ratio of the InAlN with a substitution rate of In around "x = 0.20" would be conserved inside the oxide layer. In our case, a layer by layer growth of the oxide is supposed by inducing three things: (1) oxidation of Al, more oxidizable, coming from InAlN top layers, (2) substitution of N and part of In by O atoms leading to the loss of In and N, and (3) oxidation of the remaining part of In at surface and entrapment of a N part onto interstitial N molecules. This qualitative model requires further investigations to propose a complete reactional mechanism scheme and evaluate the annealed InAlN barrier layers stability. To this end, a focus on the evolution of the N1s region with the thermal budget and ageing time is presented in the next section.

XPS investigation of the N1s spectral regions: influence of the thermal budget and ageing time.—The N chemical nature and specific position in the film organization is an important point directly related to the high temperature oxidation process of InAlN. First of all, the particular feature called "N1s (inter)" concerns the specificity of the N response with the new contribution at 404.0 eV resulting

Downloaded on 2018-09-14 to IP 193.51.24.15 address. Redistribution subject to ECS terms of use (see ecsdl.org/site/terms_use) unless CC License in place (see abstract).

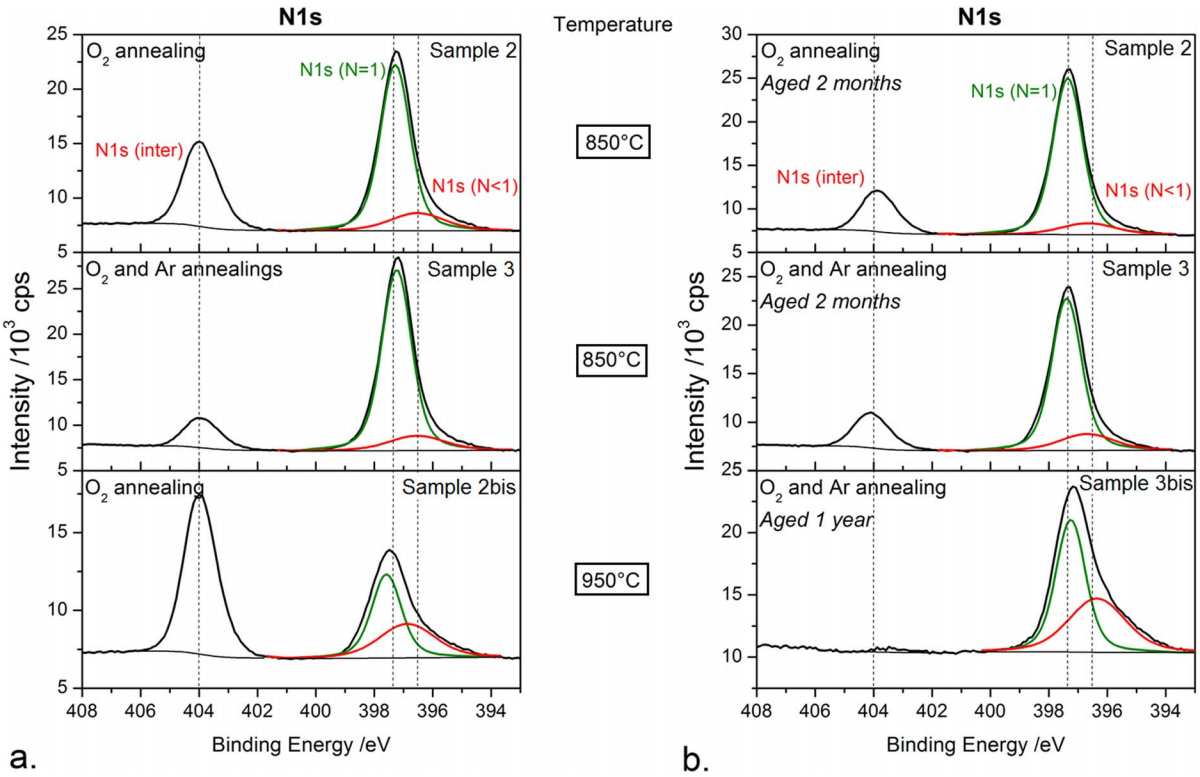

Figure 6. High energy resolution XPS spectra presenting the N1s region of, a. the annealed samples (Sample 2, 3, and 2bis), and b. the aged samples (Sample 2, 3, and 3bis).

from the O_2 annealing and appearing in Sample 2 and Sample 3 (Figure 3).

To our knowledge, such N1s XPS signature, presenting a chemical shift of 6.7 eV with respect to the "N1s (mat)" energy position, has not been reported in the literature for InAlN surfaces. A similar high binding energy contribution has been observed on InN as-deposited thin films with N excess and attributed to interstitial N_2,[68] i.e. molecular N_2 embedded in the atomic lattice close to the surface. Other studies about N_2^+ implantation in InP, InAs, or InSb III-V compounds,[64] but also in Al_2O_3 and SiO_2,[69,70] or SiON[71] report similar XPS evidences of interstitial N_2 presence and propose a pattern in which N_2 molecules are trapped in the cation deficiency sites and surrounded by O atoms bonded to metal cations.[69] Another possible attribution mentioned in the literature would be N atoms bond to O ones (N-O_2) inside the matrix. But in this case, suboxides, for example compounds containing Al-O-N bonds, are systematically detected in addition to the N1s features at 401 or 402 eV[72–76] which are not observed in the present study.

Besides this additional N1s peak at 404.0 eV, another contribution at lower energy has to be considered. As presented in Figure 4, a change of the "N1s (mat)" peak is observed after O_2 annealing and conserved after Ar annealing, with the appearance of a shoulder at lower energy, approximately at 396.5 eV. Thus, before annealing (on Sample 1), the N1s peak shape is fairly symmetric with a width (FWMH) of 1.2 eV. Therefore, a third contribution is added to adequately fit the N1s spectral envelope of the "(mat)" peak for all the other samples after the annealing and ageing steps. This contribution, characterized by a FWMH ranged between 2.2 and 2.3 eV, is visible on all annealed samples and its proportion grows with the annealing temperature (Figure 6a). Somehow, this shape could have been attributed to Ga-$L_2M_{45}M_{45}$ Auger bands, originating from Ga as reported in many papers.[77-80] However, no Ga2p core-level (∼1110–1130 eV) is detected from the XPS survey spectra, excluding here this possibility. The most probable attribution, by analogy with a similar contribution found on AlN (and in the same proportion than the one observed for Sample 2 and 3), will be the presence of N atoms in defect position in the InAlN matrix, namely "$AlN_{(x<1)}$",[58,81] extended here to "$InAlN_{(x<1)}$" under-stoichiometric species in our case. This also evidences the absence of such defects (or in a very insignificant proportion) on the as-grown and deoxidized sample (Sample 1), for which this low energy contribution is not visible. Also, in Figure 6 and Table VI, two distinct "N1s (mat)" contributions are considered and denoted as followed: "N1s (N = 1)" for the undisturbed and stoichiometric part of "$InAlN_{(x=1)}$", and "N1s (N<1)" for the structural defects and the sub-stoichiometric fraction of "$InAlN_{(N<1)}$" previously introduced.

The complementary study presented in the following part of the text aims to refine the high temperature oxidation mechanism and especially focusing on N1s specificity. First, an oxidation step at higher temperature (950°C) was realized in order to intensify the oxidation mechanism (Sample 2bis).

The comparison of the N1s regions of InAlN annealed at 850°C (O_2 and Ar, Sample 2 and 3) and 950°C (Sample 2bis) is presented in Figure 6a. The corresponding atomic concentrations obtained after N1s fitting are gathered in Table VIa. First, the "N1s (inter)" contribution is even more clearly visible on Sample 2bis showing that an increase in the O_2 annealing temperature is directly associated to a high increase of the interstitial N content. Thus, proportion of interstitial N ranges from 31.7% of the total N present at 850°C (Sample 2), up to 52.9% at 950°C (Sample 2bis). Surprisingly, the interstitial N molecules can become the dominant part of the N content with enough cohesion and short time stability (at day scale) to remain at this high level. This result was really unattended knowing that every reference reporting the "N1s (inter)" peak described it in a low fraction of the N content.[65] A possible explanation will be to consider a fraction of N physisorbed or chemisorbed inside the oxide film. Ozensoy et al.[82] have shown the high interaction of NO_x species on a surface of Al_2O_3 thin films, and investigated the higher stability of chemisorbed ionic nitrite species NO_2^-. The existence of a fraction of NO_x species chemisorbed inside the Al-rich oxide film formed after O_2 annealing would moreover explain the decrease of the "N1s (inter)" after the Ar annealing (Sample 3). Thus, the additional Ar annealing leads to

Downloaded on 2018-09-14 to IP 193.51.24.15 address. Redistribution subject to ECS terms of use (see ecsdl.org/site/terms_use) unless CC License in place (see abstract).

Table VI. Proportion of the different contributions "N1s (inter)", "N1s (N = 1)", and "N1s (N<1)" relative to the total content of N1s, and atomic ratio of N(<1) inside the InAlN matrix. Data are associated to Figure 6. The standard deviations are assumed at ± 0.1 for proportion and at ± 0.01 for the atomic ratio.

	Proportion /%			
		N1s (mat)		Atomic ratio
a.	N1s (inter)	N1s (N = 1)	N1s (N<1)	N (<1)/N (mat)
Sample 2 - 850°C (O_2)	31.7	57.2	11.1	0.19
Sample 3 - 850°C (Ar)	13.5	75.0	11.5	0.15
Sample 2bis - 950°C (O_2)	52.9	27.1	20.0	0.74
b.	Proportion /%			
		N1s (mat)		Atomic ratio
	N1s (inter)	N1s (N = 1)	N1s (N<1)	N (<1)/N (mat)
Sample 2 - Aging 2 months	20.1	70.5	9.4	0.13
Sample 3 - Aging 2 months	17.5	68.9	13.7	0.20
Sample 3bis - Aging 1 year	1.7	57.3	42.9	0.78

a decreased by a factor of 2 of the "N1s (inter)" intensity (Table IV). The main explanation of this phenomenon is that a certain amount of N molecules embedded inside the structure are relaxed with the Ar thermal treatment. This is in good agreement with the decrease of the oxide layer thickness after Ar annealing.

In addition, the generation of defects inside the InAlN matrix, evidenced by the "N1s (N<1)" contribution in Figure 6a, is also found to be related to the thermal budget, as an increasing proportion with the annealing temperature is shown. The atomic ratio "N (<1)/N (mat)", which characterizes the fraction of N defects inside the InAlN matrix (Table VI), rises from 0.19 until 0.74 at higher temperature. Then, their generation seems to follow the same trend with temperature than the one observe for the interstitial N_2. However, such important defects proportion means that the InAlN matrix is strongly perturbed, and, obviously, requires adjusting the operating temperature for an optimized HEMT fabrication process.

Then, a stability study was led, by proceeding to the XPS analysis of the two samples annealed at 850°C after two months (Sample 2 and 3) ageing in air atmosphere. The evolution after one year ageing of an extreme case: a sample representative of the whole process (O_2 and Ar annealings) at higher temperature of 950°C, and presenting initially a large amount of "N1s (inter)" is also presented.

The N1s spectral regions of the aged samples are gathered in Figure 6b, with the corresponding atomic concentrations in Table VIb and with a specific attention paid on the "N1s (inter)" and "N1s (N<1)" peaks evolution in time.

Firstly, for the 850°C process, the "N1s (inter)" proportion measured after oxidation (Sample 2) is found to decrease from 32% to 20% in two months of ageing. However, after additional Ar annealing (Sample 3), the "N1s (inter)" proportion is practically constant (passing through 13.5% to 17.5%) for a similar ageing duration. Thus, after a two-month ageing, the partial relaxation of interstitial N is only visible after the O_2 annealing, showing a stability increase after Ar treatment. Besides this observation, a relaxation of more than half of the interstitial N_2 molecules is observed after Ar treatment, ranging from 31.7% (Sample 2) to 13.5% (Sample 3) of the total N content. Such relaxation was previously mentioned and attributed to reorganization at the oxide/InAlN matrix interface where an interlayer (In and N poor) was evidenced just after the oxidation step (Table V).

Another interesting point is that, at a larger timescale (one year), almost all the interstitial N molecules are desorbed, as illustrated in the case of Sample 3bis presenting an estimated "N1s (inter)" proportion of only 1.7%, and showing a progressive and slow evacuation of the interstitial N_2.

For the three samples studied, the N defects contributions, "N1s (N<1)", do not decrease with ageing time. In fact, they seem to stay in a proportion around 15 ± 5% of the overall InAlN matrix whatever the thermal budget and ageing time considered. Even in the case where defects are present in a large majority (950°C), their proportion remains constant around 75 ± 5% even after ageing time of one year.

These observations are a strong evidence to finally attribute (1) the "N1s (inter)" component as interstitial N_2 molecules, appearing as not stable in a long timescale, trapped inside the structure with non-covalent bonds, and probably situated between the oxide layer and the $In_yAl_{(1-y)}N_{<1}$ interlayer; and (2) the "N1s (N<1)" component as N deficiencies representative of the $In_yAl_{(1-y)}N_{<1}$ interlayer, and keeping its proportion over time.

Finally, InAlN thin films are complex ternary alloys with intermediate properties between those of AlN and InN depending directly on the In content. Since experimental data on binary compounds are available in the literature,[67,83] a parallel can be drawn with the ternary compound. InAlN epitaxial layers present a strong crystal cohesion that moderate surface reactivity but O incorporation, even limited, is possible with thermic assistance. Our XPS results demonstrate that InAlN oxidation follows a layer by layer process. The oxidation film, "In-Al-O", is thin (between 2.5 nm and 3.1 nm after the O_2 annealing at 850°C), well-covering, and Al-rich. The Al surface enrichment (with a correlated In and N loss) and an interstitial N presence between the surface oxide layer and the $In_yAl_{(1-y)}N_{<1}$ interlayer show that InAlN decomposition starts well below the growth temperature for AlN (1100°C),[3] but well above the degradation temperature for InN (600°C).[39,84] One should note that the temperature of 850°C chosen here is very close to the MOVPE growth temperature of InAlN at 870°C. The minor In content (given with 20% of incorporation) present in the InAlN matrix may therefore enable the surface decomposition at a temperature of 850°C even before the O incorporation for the thermal oxide growth.[41,85]

Origin of interstitial N remains an open question. First, it can result from N atoms reorganization during oxidation. Secondly, in AlN and InN thin films, N defects,[58,68] even at the surface, are present so it cannot be excluded that such defects could also gather, leading to a N_2 interstitial formation in the oxidation film formed on InAlN. Although there is no such experimental evidence of this mechanism to InAlN ternary alloy, the molecular N_2 recombination mechanism can be proposed, as a direct transposition for N loss on InN thin films.[86] The formation of interstitial N_2, as well as its incorporation inside the "In-Al-O" surface oxide layer remains a complex issue, and it seems hazardous on the base of present results to predict with absolute certainty its origin.

Regarding from these results, one should notice that N_2 interstitial molecules are instable and need to be avoided during the fabrication of HEMT devices. The N deficiency evidenced inside the interlayer seems to be less inconvenient as strong covalent bonds linked the overall structure (oxide/interlayer/matrix). Nevertheless their relative proportion seems to be associated to N_2 content when no ageing

Downloaded on 2018-09-14 to IP 193.51.24.15 address. Redistribution subject to ECS terms of use (see ecsdl.org/site/terms_use) unless CC License in place (see abstract).

time is applied. During the industrial process, long time relaxation is not conceivable, and additional Ar annealing treatment does not fully relaxed the N_2 content. Indeed, O_2 thermal annealing at low temperature (below 850°C) has to be considered as a solution to limit the N evolution, Ar final treatment remains an essential step.

Conclusions

InAlN/GaN heterostructures have the asset to present a strong stability through air atmosphere. In this paper, we study by XPS the behavior of InAlN thin layers through the three processing steps relative to the oxidation procedure in the HEMT fabrication process. The evolution of the surface chemical composition, after ammonia pre-cleaning, to eliminate the native sub-nanometric oxide, O_2 annealing, realized to reduce the leakage current, and Ar annealing, principally acting as an healing treatment, at 850°C is presented. First, a practically deoxidized surface is evidenced after ammonia treatment, considered as the XPS reference surface. Then, the formation of an oxidation film is shown by the substantial oxygen content increase at the surface after O_2 annealing, as well as an incredibly low contamination level (< 6 at.%). But, principally the oxidation process is accompanied by the appearance of an unusual N1s fingerprint. A complete reconstruction of the main photopeaks Al2p, In3$d_{5/2}$, N1s, O1s, and C1s, is performed to precisely determine the surface chemical environments and get a better understanding on the oxidation mechanism.

After the oxidation step, a conformal and covering ultra-thin aluminium-rich oxide film of almost 3 nm is formed. This important difference in III-elements balance in the oxide film and in the InAlN matrix enables to exclude a layer by layer oxidation mechanism. The oxidation of the barrier is supposed to proceed by breaking the InAlN chemical bonds at 850°C enabling the oxygen incorporation in the InAlN top layers. The O_2 annealing is found to drastically decrease the Indium and nitrogen contents, as already referred for InN surface degradation at temperature above 600°C. We also demonstrate that the O_2 annealing leads to the creation of nitrogen defects ("N1s (N<1)" contribution at 396.5 eV), related to an under-stoichiometric InAlN network, in association with a slight decrease of the InAlN matrix stoichiometry: the "[In (mat)+Al (mat)]/N (mat)" ratio varying from 1.00 to 0.96, indicating that the matrix below the oxide film is superficially modified. Such nitrogen defects are found to increase with the thermal budget. These results attest also of the formation of a indium and nitrogen deficient substructure, "$In_yAl_{1-y}N_{(<1)}$", during oxidation, and situated between the oxide layer and the undisturbed InAlN matrix. The Ar annealing treatment plays his role of healing thermal treatment by partially re-arranging the chemistry at the interface.

One main result of this study is a characteristic XPS signature of the N1s region presenting a rather unusual feature at 404.0 eV. This contribution strongly shifted of + 6.7 eV compared to the nitrogen matrix contribution (397.3 eV) is attributed to the presence of interstitial N_2 trapped between the surface oxide film and the $In_yAl_{(1-y)}N_{<1}$ interlayer. Even if the origin of interstitial nitrogen remains an open question, different mechanisms can be proposed for the formation of interstitial N_2 with reference to previous works published on InN behavior, and proposing a reorganization of Nitrogen atoms during oxidation or defects accumulation arising from the bonds breaking during heating. By increasing the oxidation step temperature (950°C), a strong increase of the interstitial nitrogen contribution is observed, becoming the predominant part of the N1s spectral region (around 53%). To our knowledge, such behavior was not yet reported for ternary nitride materials.

This interstitial N_2 is progressively released during ageing under air and also decreased by the Ar annealing, accelerating the relaxation at the interface, although the nitrogen defects remains practically constant once they are formed even after one year ageing. It confirms that nitrogen defects are representative of the InAlN matrix, contrarily to the interstitial N_2 molecules, probably localized at the interface between the oxide and the matrix, and almost totally gone after one year. Complementary information could be obtained with the same approach but by varying the In content in InAlN. The discrete determination of in-depth distribution through the surface oxide and the interlayer by AR-XPS (Angle Resolved – XPS) is also under consideration.

Considering the HEMT process, interstitial N_2 formation has to be avoided due to their instability. A possible solution will be to consider a lower operating temperature (<850°C) for the oxidation process (O_2) including the essential Ar step or an alternative procedure such as wet chemical oxidation for which XPS is a key technique to optimize the solution formulations and finely orientate the surface chemistry.

To conclude, this study shows the strength of XPS for InAlN ultra-thin layers analysis. The 10 nm escape depth of the photoelectrons perfectly suits the barrier layer depth dimension and enables a non-destructive characterization within the whole layer giving the possibility to perform retro-engineering on high added value microelectronic devices where a quantitative feedback on the surface and interface chemistry modifications is mandatory.

Acknowledgments

This work was carried out in the framework of the VEGaN 2 Project supported by the Fond Unique Interministériel (FUI– AAP 19).

ORCID

Y. Bourlier https://orcid.org/0000-0002-0966-0342
M. Bouttemy https://orcid.org/0000-0001-5907-2576

References

1. Z. Gacevic, S. Fernandez-Garrido, J. M. Rebled, S. Estrade, F. Peiro, and E. Calleja, *Appl. Phys. Lett.*, **99**, 031103 (2011).
2. S. Nakamura, *Science*, **281**, 956 (1998).
3. N. Kriouche, A. Watanabe, O. Oda, and T. Egawa, *J. Cryst. Growth*, **390**, 51 (2014).
4. J.-F. Carlin and M. Ilegems, *Appl. Phys. Lett.*, **83**, 668 (2003).
5. J.-F. Carlin, C. Zellweger, J. Dorsaz, S. Nicolay, G. Christmann, E. Feltin, R. Butté, and N. Grandjean, *Phys. Stat. Sol. B*, **242**, 2326 (2005).
6. H. P. D. Schenk, M. Nemoz, M. Korytov, P. Vennéguès, A. D. Dräger, and A. Hangleiter, *Appl. Phys. Lett.*, **93**, 081116 (2008).
7. H. F. Liu, C. C. Tan, G. K. Dalapati, and D. Z. Chi, *J. Appl. Phys.*, **112**,063114 (2012).
8. R. Butté, J.-F. Carlin, E. Feltin, M. Gonschorek, S. Nicolay, G. Christmann, D. Simeonov, A. Castiglia, J. Dorsaz, H. J. Buehlmann, S. Christopoulos, G. Baldassarri, Höger von Högersthal, A. J. D. Grundy, M. Mosca, C. Pinquier, M. A. Py, F. Demangeot, J. Frandon, P. G. Lagoudakis, J. J. Baumberg, and N. Grandjean, *J. Phys. D: Appl. Phys.*, **40**, 6328 (2007).
9. I. M. Watson, *Coord. Chem. Rev.*, **257**, 2120 (2013).
10. T. Palacios, A. Chakraborty, S. Rajan, C. Poblenz, S. Keller, S. P. Denbaars, J. S. Speck, and U. K. Mishra, *IEEE Electron Device Lett.*, **26**, 781 (2005).
11. I. Daumiller, D. Theron, C. Gaquiere, A. Vescan, R. Dietrich, A. Wieszt, H. Leier, R. Vetury, U. K. Mishra, I. P. Smorchkova, S. Keller, N. X. Nguyen, and E. Kohn, *IEEE Electron Device Lett.*, **22**, 62 (2001).
12. J. A. del Alamo and J. Joh, *Microelectron. Reliab.*, **49**, 1200 (2009).
13. S. Pandey, D. Cavalcoli, B. Fraboni, A. Cavallini, T. Brazzini, and F. Calle, *Appl. Phys. Lett.*, **100**, 152116 (2012).
14. L. Semra, A. Telia, M. Kaddeche, and A. Soltani, *International Conference on Engineering and Technology (ICET)*, 1 (2012).
15. M. F. Romero, M. Feneberg, P. Moser, C. Berger, J. Bläsing, A. Dadgar, A. Krost, E. Sakalauskas, and R. Goldhahn, *Appl. Phys. Lett.*, **100**, 212101 (2012).
16. N. Sarazin, E. Morvan, M. A. di Forte Poisson, M. Oualli, C. Gaquiere, O. Jardel, O. Drisse, M. Tordjman, M. Magis, and S. L. Delage, *IEEE Electron Device Lett.*, **31**, 11 (2010).
17. D. Donoval, A. Chvála, R. Šramatý, J. Kováč, E. Morvan, Ch. Dua, M. A. diForte-Poisson, and P. Kordoš, *J. Appl. Phys.*, **109**, 063711 (2011).
18. J. Kuzmik, *IEEE Electron Device Lett.*, **22**, 510 (2001).
19. J. S. Xue, Y. Hao, J. C. Zhang, X. W. Zhou, Z. Y. Liu, J. C. Ma, and Z. Y. Lin, *Appl. Phys. Lett.*, **98**, 113504 (2011).
20. J. Ichikawa, Y. Sakai, Z. Chen, K. Fujita, and T. Egawa, *Jpn. J. Appl. Phys.* **51**, 01AF07 (2012).
21. E. Taylor, M. D. Smith, T. C. Sadler, K. Lorenz, H. N. Li, E. Alves, P. J. Parbrook, and R. W. Martin, *J. Cryst. Growth*, **408**, 97 (2014).
22. H. R. Brice, T. C. Sadler, M. J. Kappers, and R. A. Oliver, *J. Cryst. Growth*, **312**, 1800 (2010).
23. L. Lugani, M. A. Py, J.-F. Carlin, and N. Grandjean, *J. Appl. Phys.*, **115**, 074506 (2014).
24. K. Jeganathan, M. Shimizu, H. Okumura, Y. Yano, and N. Akutsu, *J. Cryst. Growth*, **304**, 342 (2007).

Downloaded on 2018-09-14 to IP 193.51.24.15 address. Redistribution subject to ECS terms of use (see ecsdl.org/site/terms_use) unless CC License in place (see abstract).

25. K. Jeganathan and M. Shimizu, *AIP Advances*, **4**, 097113 (2014).
26. M. H. Wong, F. Wu, C. A. Hurni, S. Choi, J. S. Speck, and U. K. Mishra, *Appl. Phys. Lett.*, **100**, 072107 (2012).
27. M. Gonschorek, J.-F. Carlin, E. Feltin, M. A. Py, and N. Grandjean, *Appl. Phys. Lett.* **89**, 062106 (2006).
28. M. Gonschorek, J.-F. Carlin, E. Feltin, M. A. Py, N. Grandjean, V. Darakchieva, B. Monemar, M. Lorenz, and G. Ramm, *J. Appl. Phys.*, **103**, 093714 (2008).
29. A. Redondo-Cubero, K. Lorentz, R. Gago, N. Gago, M.-A. diForte Poisson, E. Alves, and E. Munoz, *J. Phys. D Appl. Phys.*, **43**, 55406 (2010).
30. D. Maier, M. Alomari, N. Grandjean, J.-F. Carlin, M.-A. diForte-Poisson, C. Dua, S. Delage, and E. Kohn, *IEEE Electron Device Lett.*, **33**, 985 (2012).
31. F. Medjdoub, J. F. Carlin, M. Gonschorek, E. Feltin, M. A. Py, D. Ducatteau, C. Gaquiere, N. Grandjean, and E. Kohn, *IEDM Tech. Dig.*, 1 (2006).
32. F. Medjdoub, M. Alomari, J.-F. Carlin, M. Gonschorek, E. Feltin, M. A. Py, N. Grandjean, and E. Kohn, *IEEE Electron Device Lett.*, **29**, 5 (2008).
33. L. Lugani, J.-F. Carlin, M. A. Py, and N. Grandjean, *Appl. Phys. Lett.*, **105**, 112101 (2014).
34. H. Yu, M. Ozturk, P. Demirel, H. Cakmak, B. Bolukbas, D. Caliskan, and E. Ozbay, *Semicond. Sci. Technol.*, **26**, 085010 (2011).
35. H. Behmenburg, L. R. Khoshro, C. Mauder, N. Ketteniss, K. H. Lee, M. Eickelkamp, M. Brast, D. Fahle, J. F. Woitok, A. Vescan, H. Kalisch, M. Heuken, and R. H. Jansen, *Phys. Status Solidi C*, **7**, 2104 (2010).
36. K. Takhar, U. P. Gomes, K. Ranjan, S. Rathi, and D. Biswas, *IOP Conf. Ser.: Mater. Sci. Eng.*, **73**, 012001 (2015).
37. Z. Y. Fan and N. Newman, *Mater. Sci. Eng. B*, **87**, 244 (2001).
38. R. D. Jones and K. Rose, *J. Phys. Chem. Sol.*, **48**, 587 (1987).
39. Q. Guo, O. Kato, and A. Yoshida, *J. Appl. Phys.*, **73**, 7969 (1993).
40. Y. Huang, H. Wang, Q. Sun, J. Chen, J. F. Wang, Y. T. Wang, and H. Yang, *J. Cryst. Growth*, **281**, 310 (2005).
41. J. Palisaitis, C.-L. Hsiao, L. Hultman, J. Birch, and P. O. A. Persson, *Acta Materialia*, **61**, 4683 (2013).
42. J. Palisaitis, C.-L. Hsiao, L. Hultman, J. Birch, and P. O. A. Persson, *Scientific Reports*, **7**, 44390 (2017).
43. A. Watanabe, J. J. Freedsman, Y. Urayama, D. Christy, and T. Egawa, *J. Appl. Phys.*, **118**, 235705 (2015).
44. J. Lee, M. Yan, B. Ofuonye, J. Jang, X. Gao, S. Guo, and I. Adesida, *Phys. Status Solidi A*, **208**, 1538 (2011).
45. G. Pozzovivo, J. Kuzmik, C. Giesen, M. Heuken, J. Liday, G. Strasser, and D. Pogany, *Phys. Status Solidi C*, **6**, S999 (2009).
46. Y. Liu, S. P. Singh, Y. J. Ngoo, L. M. Kyaw, M. K. Bera, Q. Q. Lo, and E. F. Chor, *J. Vac. Sci. Technol.*, **B32**, 032201 (2014).
47. M. Alomari, A. Chuvilin, L. Toth, B. Pecz, J.-F. Carlin, N. Grandjean, C. Gaquière, M.-A. di Forte-Poisson, S. Delage, and E. Kohn, *Phys. Status Solidi C*, **7**, 13 (2010).
48. S. Ozaki, K. Makiyama, T. Ohki, Y. Kamada, M. Sato, Y. Niida, N. Okamoto, and K. Joshin, *Phys. Status Solidi A*, **213**, 1259 (2015).
49. J. Kováč, R. Šramatý, A. Chvála, H. Sibboni, E. Morvan, M. A. diForte-Poisson, D. Donoval, and P. Kordoš, *Appl. Phys. Lett.*, **98**, 162111 (2011).
50. M. Eickelkamp, M. Weingarten, L. Rahimzadeh Khoshoroo, N. Ketteniss, H. Behmenburg, M. Heuken, D. Donoval, A. Chvála, P. Kordoš, H. Halisch, and A. Vescan, *J. Appl. Phys.*, **110**, 084501 (2011).
51. T. Hashizume and H. Hasegawa, *Appl. Surf. Sci.*, **234**, 387 (2004).
52. M. Akazawa and T. Nakano, *ECS Solid State Letters*, **1**, P4 (2012).
53. M. Akazawa, M. Chiba, and T. Nakano, *CS MANTECH Conference*, Denver, Colorado, USA (2014).
54. S. W. King, J. P. Barnak, M. D. Bremser, K. M. Tracy, C. Ronning, R. F. Davis, and R. J. Nemanich, *J. Appl. Phys.*, **84**, 5248 (1998).
55. J. Choi, R. Puthenkovilakam, and J. P. Chang, *Appl. Phys. Lett.*, **86**, 192101 (2005).
56. M. R. Alexander, G. E. Thompson, and G. Beamson, *Surf. Interface Anal.*, **29**, 468 (2000).
57. I. Bertoti, *Surf. Coat. Technol.*, **151–152**, 194 (2002).
58. L. Rosenberger, R. Baird, E. McCullen, G. Auner, and G. Shreve, *Surf. Interface Anal.*, **40**, 1254 (2008).
59. Y.-H. Chang, Y.-S. Lu, Y.-L. Hong, C.-T. Kuo, S. Gwo, and J. A. Yeh, *J. Appl. Phys.*, **107**, 043710 (2010).
60. R. Zhang, P. Zhang, T. Kang, H. Fan, X. Liu, S. Yang, H. Wei, Q. Zhu, and Z. Wang, *Appl. Phys. Lett.*, **91**, 162104 (2007).
61. T. Nagata, G. Koblmüller, O. Bierwagen, C. S. Gallinat, and J. S. Speck, *Appl. Phys. Lett.*, **95**, 132104 (2009).
62. E. O. Filatova and A. S. Konashuk, *J. Phys. Chem. C*, **119**, 20755 (2015).
63. M. Alizadeh, V. Ganesh, B. T. Goh, C. F. Dee, A. R. Mohmad, and S. A. Rahman, *Appl. Surf. Sci.* **378**, 150 (2016).
64. J. D. Hecht, F. Forst, T. Chassé, D. Hirsch, H. Neumann, A. Schindler, and F. Bigl, *Appl. Surf. Sci.*, **179**, 196 (2001).
65. S. Tanuma, C. J. Powell, and D. R. Penn, *Surf. Interface Anal.*, **21**, 165 (1994).
66. C. J. Powell and A. Jablonski, National Institute of Standards and Technology, *Standard Reference Database* **71**, (2010).
67. J. Hong, J. W. Lee, C. B. Vartuli, J. D. MacKenzie, S. M. Donovan, C. R. Abernathy, R. V. Crockett, S. J. Pearton, J. C. Zolper, and F. Ren, *Solid State. Electronics*, **41**, 681 (1997).
68. K. S. Butcher, A. J. Fernandes, P. P.-T. Chen, M. Wintrebert-Fouquet, H. Timmers, S. K. Shrestha, H. Hirshy, R. M. Perks, and B. F. Usher, *J. Appl. Phys.*, **101**, 123702 (2007).
69. J. P. Espinós, A. R. González-Elipe, M. Mohai, and I. Bertóti, *Surf. Interface Anal.*, **30**, 90 (2000).
70. I. Bertoti, *Catal. Today*, **181**, 95 (2012).
71. Y. Chung, J. C. Lee, and H. J. Shin, *Appl. Phys. Lett.*, **86**, 022901 (2005).
72. M. Losurdo, P. Capezzuto, and G. Bruno, *J. Appl. Phys.*, **88**, 2138 (2000).
73. H. Shinoda and N. Mutsukura, *Dia. Relat. Mater.*, **11**, 896 (2002).
74. G. V. Soares, K. P. Bastos, R. P. Pezzi, L. Miotti, C. Driemeier, I. J. R. Baumvol, C. Hinkle, and G. Lucovsky, *Appl. Phys. Lett.*, **84**, 4992 (2004).
75. P. W. Wang, J.-C. Hsu, Y.-H. Lin, and H.-L. Chen, *Appl. Surf. Sci.*, **256**, 4211 (2010).
76. P. W. Wang, J. C. Hsu, Y. H. Lin, and H. L. Chen, *Surf. Interface Anal.*, **43**, 1089 (2011).
77. N. Karar, R. Opila, and T. Beebe Jr., *J. Electrochem. Soc.*, **158**, D342 (2011).
78. M. D. Smith, E. Taylor, T. C. Sadler, V. Z. Zubialevich, K. Lorenz, H. N. Li, J. O'Connell, E. Alves, J. D. Holmes, R. W. Martin, and P. J. Parbrook, *J. Mater. Chem. C*, **2**, 5787 (2014).
79. L. Wang, Y. Bu, and J.-P. Ao, *Diam. Relat. Mater.*, **73**, 1 (2017).
80. R. Bouveyron and M. B. Charles, *J. Cryst. Growth*, **464**, 105 (2017).
81. N. Laidani, L. Vanzetti, M. Anderle, A. Basillais, C. Boulmer-Leborgne, and J. Perriere, *Surf. Coati. Technol.*, **122**, 242 (1999).
82. E. Ozensoy, C. H. F. Peden, and J. Szanyi, *J. Phys. Chem. B*, **109**, 15977 (2005).
83. O. Ambacher, *J. Phys. D: Appl. Phys.*, **31**, 2653 (1998).
84. K. P. Biju and M. K. Jain, *J. Cryst. Growth*, **311**, 2542 (2009).
85. S. V. Ivanov, T. V. Shubina, T. A. Komissarova, and V. N. Jmerik, *J. Cryst. Growth*, **403**, 83 (2014).
86. K. S. Butcher, P. P.-T Chen, and J. E. Downes, *Appl. Phys. Lett.*, **100**, 011913 (2012).

Downloaded on 2018-09-14 to IP **193.51.24.15** address. Redistribution subject to ECS terms of use (see **ecsdl.org/site/terms_use**) unless CC License in place (see abstract).